

Estimation of ages and masses via carbon and nitrogen abundances for 556 007 giants from LAMOST

Xu Zhang^{1,2}, Sven Buder^{3,4}, Ya-Qian Wu¹ and Gang Zhao^{1,2}

¹ CAS Key Laboratory of Optical Astronomy, National Astronomical Observatories, Chinese Academy of Sciences, Beijing 100101, China; gzhao@nao.cas.cn

² School of Astronomy and Space Science, University of Chinese Academy of Sciences, Beijing 100049, China

³ Research School of Astronomy & Astrophysics, Mount Stromlo Observatory, Australian National University, ACT 2611, Australia

⁴ Center of Excellence for Astrophysics in Three Dimensions (ASTRO-3D), Australia

Received 2021 March 16; accepted 2021 April 20

Abstract Estimating ages for a large number of giants is of great importance for studying Galactic evolution. In this work, we determine stellar ages and masses for 556 007 giants from LAMOST Data Release 5 (DR5) with empirical relations estimated from chemical [C/N] abundance ratios. Our sample reveals the two well-known sequences in the age– $[\alpha/M]$ relation. The high- α sequence is composed of stars older than 8 Gyr and low- α sequence is composed of stars with age ranging from 0 Gyr to 13.8 Gyr. Our sample also shows a flat age– $[M/H]$ relation up until 12 Gyr. We compare these distributions with Galactic Chemical Evolution models for reference. When looking at the spatial distribution of stars in 2 Gyr age bins, we find that young stars are concentrated towards the Galactic plane and older stars extend to higher height above and below the disk. We find a smooth transition of median Galactic height for different age bins, which suggests a strong age-dependence on Galactic scale height.

Key words: stars: fundamental parameters — Galaxy: structure — Galaxy: evolution — Galaxy: abundances

1 INTRODUCTION

Obtaining accurate and precise ages for large numbers of stars is important for understanding the Milky Way evolution. Stellar age, together with mass and metallicity, is one of the key parameters to determine the evolutionary state of a star. However, it cannot be measured directly from observations and is always model-dependent (e.g., [Soderblom 2010](#)).

A practical way to measure ages for large samples of stars is to determine their position on the Hertzsprung-Russell Diagram (HRD). This method yields precise ages for stars at the main-sequence turn-off and on the subgiant branch in regions of the HRD. However, the method is less precise for determining ages for giants, as isochrones of giants with different ages are close in temperature and color space. Due to their high luminosity, giants are crucial probes of the structure of the Milky Way, especially for the distant halo. Thus age estimates for giants are of enormous importance. Modern large scale surveys, such

as the Large sky Area Multi-Object Fiber Spectroscopic Telescope (LAMOST; [Zhao et al. 2006, 2012](#); [Cui et al. 2012](#)) survey, the Apache Point Observatory Galactic Evolution Experiment (APOGEE; [Majewski et al. 2017](#)) and Galactic Archaeology with HERMES (GALAH; [De Silva et al. 2015](#)), have obtained high-quality spectra for a large number of giants, which allow the derivation of detailed stellar chemical compositions. To unlock the chemical/chemodynamical evolution of the Milky Way, it is also vital to estimate stellar ages.

[Masseron & Gilmore \(2015\)](#) and [Martig et al. \(2016\)](#) have shown that the photospheric ratio of [C/N] changes depending on stellar mass during the post-main-sequence evolution as a result of dredge-up. Based on measurements from APOGEE, [Martig et al. \(2016\)](#) demonstrated that masses of red giants can be predicted from photospheric carbon and nitrogen abundances as well as spectroscopic stellar labels T_{eff} , $\log g$ and $[M/H]$. They also established an empirical relation between these quantities with seismic mass and subsequently also age estimates by 1475 red

giants from the *Kepler* mission (Borucki et al. 2010). With this empirical model, they estimated masses and ages for $\sim 52\,000$ stars in APOGEE Data Release 12 (DR12) (Majewski et al. 2017). Ho et al. (2017b) excellently applied the empirical relation established by Martig et al. (2016) to LAMOST Data Release 2 (DR2) and estimated ages for a large sample of 230 000 giants. Using the APOKASC (Pinsonneault et al. 2014) sample as a training set, Ness et al. (2016) accurately estimated ages and masses for $\sim 70\,000$ APOGEE red giants with *The Cannon*. Wu et al. (2018) deduced ages and masses from LAMOST spectra with a machine learning method named Kernel Principal Component Analysis (KPCA), which means we can directly estimate age and mass from spectra, taking red giant branch (RGB) stars from *Kepler* as the training dataset, and they also explored the feasibility of estimating ages and masses based on spectroscopically measured carbon and nitrogen abundances and established an empirical relation to derive mass and age by carbon and nitrogen abundances. Sharma et al. (2020) greatly explored the dependence of elemental abundances on stellar age and metallicity among Galactic disk stars with data from the third data release of GALAH (Buder et al. 2021). Zhang et al. (2019) determined stellar parameters and α , C, N abundances with deep learning for 938 720 giants, as part of LAMOST Data Release 5 (DR5), for which the empirical formulae can be applied to estimate ages and masses for this even larger sample of giants.

The paper is arranged as follows. In Section 2, we introduce the LAMOST survey and its stellar parameters. We select a subsample from these data, which is suitable for the empirical formula by Wu et al. (2018). In Section 3, we estimate ages and masses for 556 007 giants based on C and N abundances with said empirical relation and compare our results with masses and ages from the literature. In Section 4, we explore age– $[\alpha/M]$ and $-[M/H]$ relations with this large sample, and detect spatial distribution of these stars in different age bins. In Section 5, we discuss our data in view of Galactic Chemical Evolution models. We also explore Galactic vertical scale height as a function of age, and we display age-abundance gradients with Galactic height. Finally, we give conclusions in Section 6.

2 DATA

2.1 The LAMOST Survey

The LAMOST survey is a low-resolution ($R \sim 1800$) optical (3700–9000 Å) spectroscopic survey (Zhao et al. 2006, 2012; Cui et al. 2012). It can collect 4000 fiber spectra in a wide field (5°) simultaneously. LAMOST has

collected a total of 9 026 365 spectra in DR5 (see <http://dr5.lamost.org/>).

2.2 Stellar Parameters

There are several different ways to estimate stellar parameters from LAMOST spectra. The LAMOST Stellar Parameter Pipeline (LASP, Luo et al. 2015; Wu et al. 2011) relied on the Correlation Function Initial method to guess the initial values of the parameters and then implemented the UlySS method (Koleva et al. 2009; Wu et al. 2011) to generate the final parameters. Ho et al. (2017a) used the data-driven method *The Cannon* to derive stellar parameters through training based on APOGEE labels. Zhang et al. (2019) determined stellar atmospheric parameters and α , C, N elemental abundances for 938 720 giants from LAMOST DR5 with a deep learning method named *StarNet* (Fabbro et al. 2018; O’briain et al. 2021). In this work, we will utilize stellar parameters from Zhang et al. (2019) to derive reliable stellar age and mass.

Before using stellar parameters from Zhang et al. (2019), we firstly compare the data with those from Xiang et al. (2017b) which were used in Wu et al. (2018) to confirm that the data are on the same scale, and if this approach is applicable for the empirical relation by Wu et al. (2018). In Figure 1, we display a comparison between the data by Zhang et al. (2019), applying *StarNet*, and Xiang et al. (2017b), applying KPCA. There are 433 523 stars for comparison, where “bias” represents the median value of residuals and “scatter” signifies the standard deviation of residuals. The bias is -55 K for T_{eff} , 0.02 dex for $\log g$, 0.00 dex for $[M/H]$, 0.00 dex for $[\alpha/M]$, 0.025 dex for $[C/H]$ and -0.115 dex for $[N/H]$. The scatter is 152 K for T_{eff} , 0.24 dex for $\log g$, 0.16 dex for $[M/H]$, 0.05 dex for $[\alpha/M]$, 0.16 dex for $[C/H]$ and 0.17 dex for $[N/H]$. In the $[\alpha/M]$ comparison map, there are few stars with $[\alpha/M] < 0.0$ dex in Zhang et al. (2019). Distribution of training set is inhomogeneous in Zhang et al. (2019). There are absolutely and relatively few stars below $[\alpha/M] < 0.0$ dex in the training set. In panel g), $[C/N]$, which is used to derive mass and age, is also compared, showing a bias of 0.14 dex and a scatter of 0.14 dex. While the bias is significant, it is constant. Therefore, we simply apply a bias correction so that our data are now on the same scale.

2.3 Quality Cuts

Zhang et al. (2019) determined stellar atmospheric parameters and α , C, N elemental abundances for 938 720 giants from LAMOST DR5. The relation by Wu et al. (2018) is however only applicable for a subset of these stars, which is stellar disk giants. Following the selection by Ho et al. (2017b), we apply quality cuts to our

data, as listed below. It leaves 556 007 objects which are suitable for the empirical formula in Wu et al. (2018). We derive $[(C + N)]/M$ with $[(C + N)/M] = [(C + N)/H] - [M/H]$ where $[(C + N)/H] = \log 10\{[10^{[C/H]} \times (N_{C_\odot}/N_{H_\odot}) + 10^{[N/H]} \times (N_{N_\odot}/N_{H_\odot})]/[(N_{C_\odot} + N_{N_\odot})/N_{H_\odot}]\} = \log 10[(10^{[C/H]} \times 10^{-3.61} + 10^{[N/H]} \times 10^{-4.21})/(10^{-3.61} + 10^{-4.21})]$. We rely on $A(C) - 12 = -3.61 = \log 10(N_{C_\odot}/N_{H_\odot})$ and $A(N) - 12 = -4.21 = \log 10(N_{N_\odot}/N_{H_\odot})$ values from Asplund et al. (2009) as reference.

$$\text{Quality Cuts} \begin{cases} -0.8 \text{ dex} < [M/H] < 0.25 \text{ dex} \\ 4000 \text{ K} < T_{\text{eff}} < 5000 \text{ K} \\ 1.8 \text{ dex} < \log g < 3.3 \text{ dex} \\ -0.25 \text{ dex} < [C/M] < 0.15 \text{ dex} \\ -0.1 \text{ dex} < [N/M] < 0.45 \text{ dex} \\ -0.05 \text{ dex} < [\alpha/M] < 0.3 \text{ dex} \\ -0.1 \text{ dex} < [(C + N)/M] < 0.15 \text{ dex} \\ -0.6 \text{ dex} < [C/N] < 0.2 \text{ dex} \end{cases} \quad (1)$$

3 ANALYSIS

3.1 Estimating Age and Mass from C and N Abundances

Wu et al. (2018) estimate age and mass based on the $[C/H]$ and $[N/H]$ abundance with a polynomial regression method. They assume a quadratic function between the age or mass and the stellar parameters: age or mass = $f(T_{\text{eff}}, \log g, [M/H], [C/N], [C/M])$. Coefficients of the fits are listed in table 2b and table 3b in Wu et al. (2018). We apply the same relation to our data selected as described in Section 2.

From Figure 1, we can see small systematic deviation (bias) between measurements from Zhang et al. (2019) and those used by Wu et al. (2018), that is from Xiang et al. (2017b). These biases are mainly only offsets. Therefore, we apply these median biases as annotated in Figure 1 onto our data when plugging them into the empirical formula to make it consistent with the KPCA ones.

3.2 Age and Mass Distribution of the Sample

Figure 2 displays histograms of the derived age and mass estimates for these stars. Panel a) affirms that the sample covers the whole range of possible ages of stars from zero on the young end to the age of universe (~ 13.8 Gyr). There are also a small number of stars with unphysical ages, i.e., younger than 0 Gyr and older than 13.8 Gyr. This is mostly caused by parameter errors in either stellar parameters or C, N abundances, which can lead to unphysical ages in empirical quadratic relations. The peak of the age distribution is at ~ 3 Gyr. The 5th, 50th and 95th percentiles

are at -0.08 Gyr, 3.79 Gyr and 8.59 Gyr, respectively. In panel b), we can see most of the stars have mass between $0.8 M_\odot - 2.6 M_\odot$. The peak is at $1.4 M_\odot$. The 5th, 50th and 95th percentiles are at $1.09 M_\odot$, $1.45 M_\odot$ and $2 M_\odot$, respectively.

3.3 Comparison with Age and Mass from the Literature

Wu et al. (2018) also estimated ages and masses from LAMOST spectra with the KPCA method. The latter is a non-linear method that extracts principal components from high-dimensional data and was applied to a different set of stellar parameters estimated for the LAMOST stars. There are 151 908 objects in common between our estimates and KPCA estimates, and we compare them in Figure 3. We find a generally good agreement between both methods, with a median bias of 1.1 Gyr for age and $-0.06 M_\odot$ for mass. This corresponds to median biases of 15.9% in age and 5.2% in mass. The scatter within the estimates is 2.4 Gyr and $0.3 M_\odot$, which is 33.1% and 19.0% respectively. While this comparison demonstrates that the absolute age values are contentious, it confirms that our ages are agreeing very well on a relative scale. Wu et al. (2019) also estimate ages for stars from LAMOST with C and N abundances. We compare our ages with those from Wu et al. (2019). Ages of 135 151 stars are compared. The median bias is 0.38 Gyr, mean bias is 0.42 Gyr and scatter is 2.38 Gyr. These values are very reasonable.

Martig et al. (2016) estimate age and mass for 52 286 stars from APOGEE DR12 and Ness et al. (2016) estimate age and mass for 73 180 stars from APOGEE DR12. So, we compare our values of age and mass with ones from Martig et al. (2016) and Ness et al. (2016). Figure 4 depicts the comparison results. When we compare our values with ones from Martig et al. (2016), 11 067 common stars are used for comparison. For age, bias is 1.00 Gyr and scatter is 2.77 Gyr. For mass, bias is $0.015 M_\odot$ and scatter is $0.19 M_\odot$. When we compare our values with ones from Ness et al. (2016), 118 common stars are considered for comparison. Bias is 1.45 Gyr and scatter is 3.00 Gyr for age, and bias is $0.06 M_\odot$ and scatter is $0.19 M_\odot$ for mass. Again, we see that the absolute values of age disagree, even more significantly here than in the comparison with Wu et al. (2018). However, the difference between both estimates can be described well by a small linear bias, confirming that our ages follow the same relative trend.

3.4 Spatial Information

We can get photogeometric distances from Bailer-Jones et al. (2021), proper motions from Gaia Early Data Release 3 (EDR3) (Gaia Collaboration et al. 2020) and

radial velocity from LAMOST DR5 v1 version catalog for 419038 stars in our sample. Combining all these parameters, we calculate three-dimensional (3D) Galactic coordinates (X, Y, Z) and galactocentric distance (R) of these stars with orbit function from *galpy* (Bovy 2015). Equatorial input such as right ascension (R.A.), declination (Decl.), distance, proper motion in R.A. direction, proper motion in Decl. direction and radial velocity are fed into the function. We define the distance of the Sun from the Galactic center as 8.178 kpc (Gravity Collaboration et al. 2018) and the distance of the Sun from the Galactic plane as 25 pc (Bland-Hawthorn & Gerhard 2016). We use the solar $(U, V, W)_{\odot} = (11.1, 12.24, 7.25)$ km s⁻¹ from Schoenrich et al. (2010). Based on the apparent motion of Sgr A* (6.379 mas yr⁻¹) with respect to the Sun, estimated by Reid & Brunthaler (2004), we then estimate the circular velocity to be 235.1 km s⁻¹. An example of ten stars in our sample is listed in Table 1 and the whole table is available online.

4 RESULTS

4.1 Correlations among Age, Metallicity and Abundances

We explore possible correlations among age, metallicity and $[\alpha/M]$ abundances. In Figure 5, we plot the distributions of stars in the age– $[\alpha/M]$ and age– $[M/H]$ planes. In the age– $[\alpha/M]$ plane, the majority of stars with solar $[\alpha/M]$ are located from 0 Gyr to 8 Gyr and stars older than 10 Gyr have typically enhanced α -abundance. Stars in the low- α part exhibit an extensive age distribution from 0 Gyr to 13.8 Gyr, but with a steep drop above 10 Gyr. The high- α part is mainly composed of stars older than 8 Gyr and ages of stars increase with the increase of $[\alpha/M]$. This distribution is similar to that found by Wu et al. (2018), while the $[\alpha/M]$ comes from different methods. We note that our sample also includes some young stars (< 8 Gyr) with high $[\alpha/M]$ values (> 0.15 dex) which are called young $[\alpha/M]$ -rich stars. The shaded area is where the young $[\alpha/M]$ -rich stars are located, which is the same as Chiappini et al. (2015). There are 18420 (4.3%) young $[\alpha/M]$ -rich stars in our sample. The relative number of young $[\alpha/M]$ -rich stars reported by Chiappini et al. (2015) is 4.5% in their sample. Possible explanations of their origin are that they were formed near the ends of the Galactic bar (Chiappini et al. 2015) or they are merger products.

In the age– $[M/H]$ panel of Figure 5, we see a large dispersion of ages across the metallicity range in our sample (-0.75 dex < $[M/H]$ < 0.25 dex) and no clear correlation. There is a flat age– $[M/H]$ relation up until 12 Gyr which is consistent with previous work using solar

neighborhood stars (Nordstrom et al. 2004; Bergemann et al. 2014). It is probably caused by radial migration (Sellwood & Binney 2002) that mixes stars born at various positions with different $[M/H]$, yielding the complex star formation and chemical enrichment history of the Galactic disk.

Figure 6 displays the number density distribution in the $[M/H]$ – $[\alpha/M]$ plane for stars in different age bins. In panel a), we show all stars from 0 Gyr – 13.8 Gyr in the $[M/H]$ – $[\alpha/M]$ panel. The plot features two prominent sequences of chemical composition. This double sequence feature is consistent with the thin and thick disk sequence (Fuhrmann 1998; Bensby et al. 2003; Lee et al. 2011; Haywood et al. 2013; Hayden et al. 2015; Xiang et al. 2017b). Stars in the thick disk have high $[\alpha/M]$ and low $[M/H]$ values, while stars in the thin disk have low $[\alpha/M]$ and high $[M/H]$ values. It has therefore been proposed (see e.g., Bland-Hawthorn et al. 2019) to rename the populations to low- α and high- α disk or sequences. As the age increases from 0 Gyr – 2 Gyr to 12 Gyr – 13.8 Gyr, the number density of the thin disk is decreasing but the number density of the thick disk is increasing. In the first 0 Gyr – 2 Gyr panel, a clear sequence is at $[M/H] \sim 0.0$ dex and $[\alpha/M] \sim 0.0$ dex. Then, in the 2 Gyr – 4 Gyr panel, the distribution widens towards lower $[M/H]$ and higher $[\alpha/M]$ and reaches the upper limit of $[M/H] = 0.25$ dex for our data on the metal-rich end. As stars get older, more and more stars appear at $[M/H] \sim -0.5$ dex and $[\alpha/M] \sim 0.2$ dex until 10 Gyr – 12 Gyr. We can clearly see one sequence of high- α up to $[\alpha/M] \sim 0.2$ dex in the 10 Gyr – 12 Gyr panel. Stars in the high- α sequence overlap those from the low- α sequence in the solar and super-solar metallicity regime. However, we confirm the finding by Buder et al. (2019), who found that one can tell apart the sequences down to the age uncertainty, when considering chemistry and age. In the 12 Gyr – 13.8 Gyr panel, only the sequence at $[M/H] \sim -0.5$ dex and $[\alpha/M] \sim 0.2$ dex can be seen. In our sample, we found a typical scatter of 2.4 Gyr from the literature comparison, suggesting that a separation into low- α and high- α sequence via age and chemistry with our sample is only uncertain for the 8 Gyr – 10 Gyr bin.

4.2 Spatial Distribution of Stars with Different Ages

Figure 7 shows the number density distribution in the $R - Z$ plane for stars in different age bins. Here R is the projected Galactocentric distance, and Z is the height above the disk midplane. Panel a) displays the number density distribution of all stars in the $R - Z$ plane. We can see lots of stars are distributed in the range of -3 kpc < Z < 3 kpc, 8 kpc < R < 16 kpc. The number of stars becomes less higher than 3.0 kpc in the Z direction and

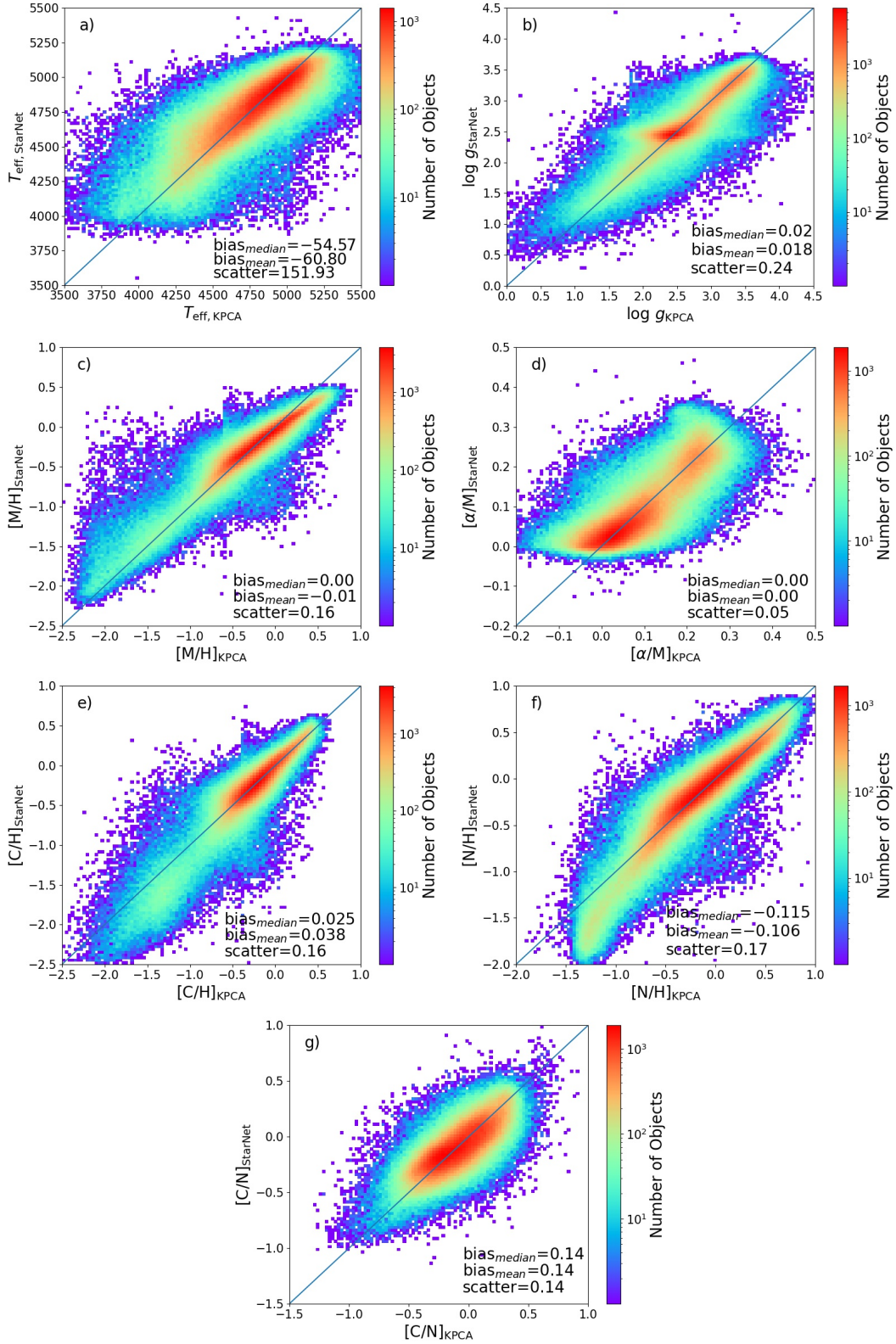


Fig. 1 Comparison of stellar parameters from Zhang et al. (2019) with those from Xiang et al. (2018). T_{eff} , $\log g$, $[M/H]$, $[\alpha/M]$, $[C/H]$ and $[N/H]$ are compared. We also compare $[C/N]$ which is used to derive age and mass in the panel g). $[C/N]$ is calculated with $[C/N] = [C/H] - [N/H]$. Bias and scatter for each parameter are marked in the corresponding panel. Colors represent number density. “Bias” represents median or mean value of residuals and “scatter” corresponds to standard deviation of residuals. We have to shift the data with the median biases shown in each panel.

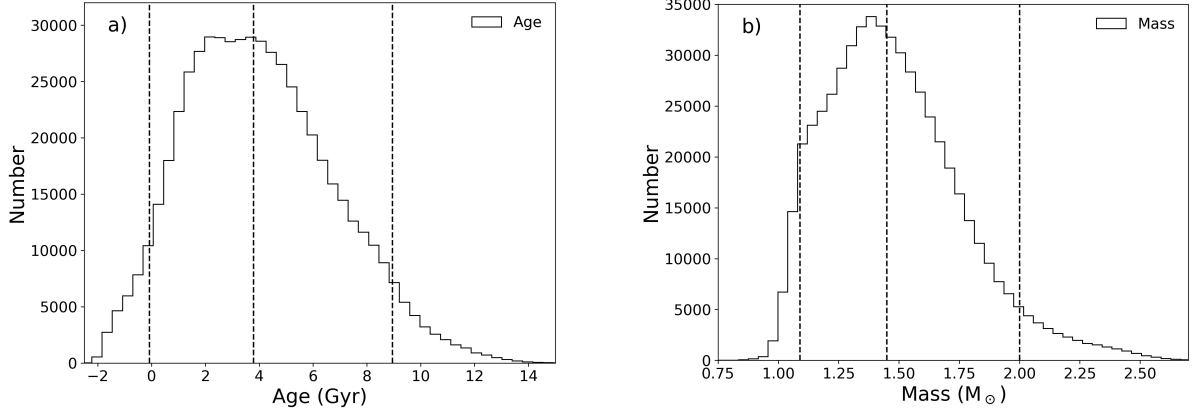


Fig. 2 Histograms of derived age and mass estimates for 556 007 stars. *Dashed lines* represent the 5th, 50th and 95th percentiles, from left to right respectively.

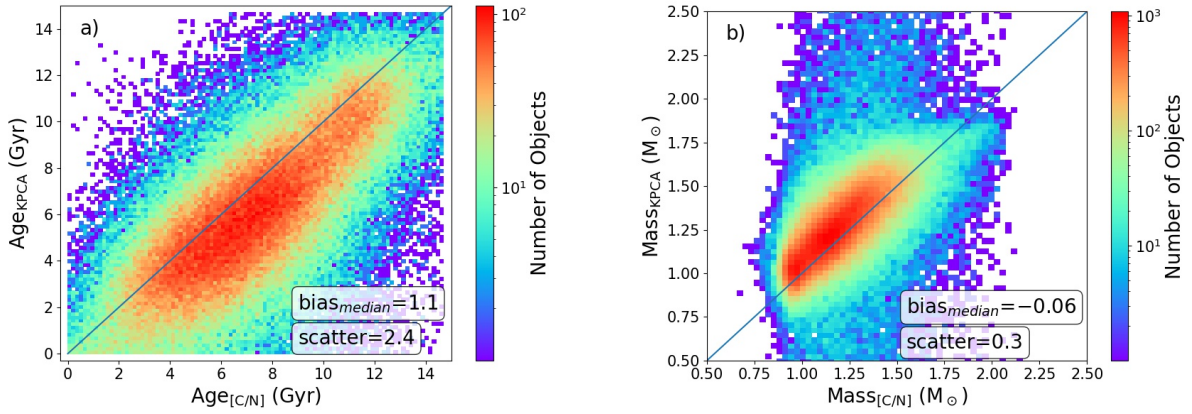


Fig. 3 Panel a): comparison of our age estimates with ones from KPCA. Bias is 1.1 Gyr and scatter is 2.4 Gyr. Panel b): same as panel a), but for mass comparison. Bias is $-0.06 M_{\odot}$ and scatter is $0.3 M_{\odot}$. Colors represent number density.

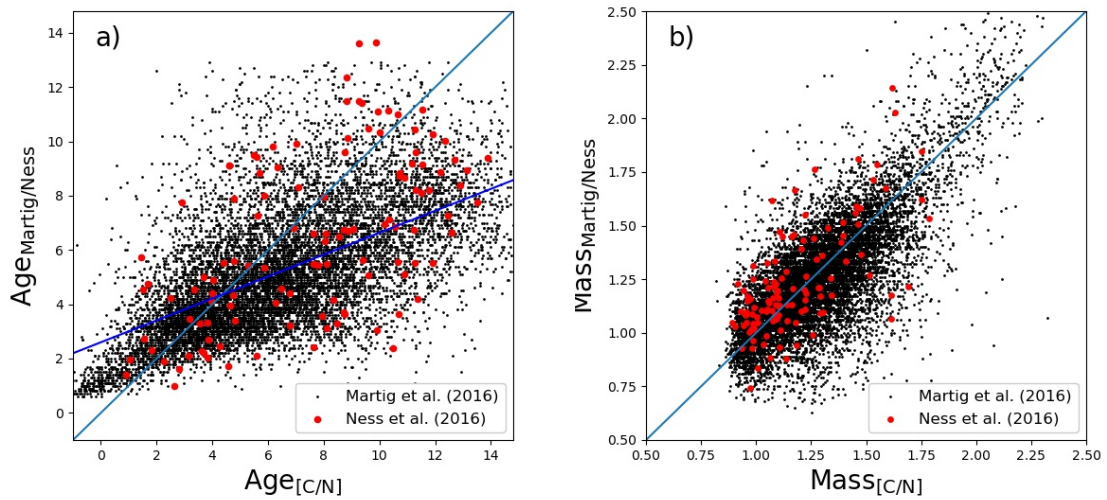


Fig. 4 Panel a): comparison of our age estimates with ones from [Martig et al. \(2016\)](#) and [Ness et al. \(2016\)](#). The *black dots* represent comparison between our estimates and ones from [Martig et al. \(2016\)](#) and the *red dots* signify comparison between our estimates and ones from [Ness et al. \(2016\)](#). The *blue line* delineates a linear fit for the *black dots* with $\text{age}_{\text{Martig}} = 2.6 + 0.4 \text{ age}_{\text{C/N}}$. Panel b): same as panel a), but for mass comparison.

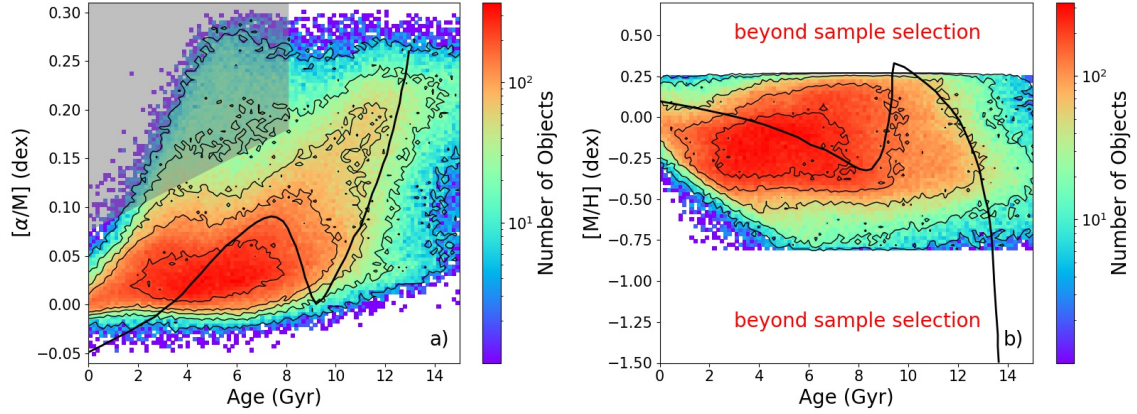


Fig. 5 Detections of age– $[\alpha/M]$ and age– $[M/H]$ relations with the sample stars. Panel a): age– $[\alpha/M]$ relation. *Black line* indicates revised two-infall model from Spitoni et al. (2019). The shaded area corresponds to where the young $[\alpha/M]$ –rich stars are located from Chiappini et al. (2015). Colors signify number density and contour lines are also shown. Panel b): same as panel a), but for age– $[M/H]$ relation.

the number of stars also becomes less further than 16 kpc in the R direction. In the 0 Gyr – 2 Gyr panel, these early stars are concentrated on the midplane in the range of $-1.5 \text{ kpc} < Z < 1.5 \text{ kpc}$. Moreover, a small number of young stars are distributed higher than $|Z| > 2.5 \text{ kpc}$. This means most of the young stars are born at the midplane. There is no obvious number density change in the R direction from 8 kpc to 13 kpc and the number density becomes smaller from 13 kpc to 17 kpc. In the 2 Gyr – 4 Gyr panel, an obvious difference from the 0 Gyr – 2 Gyr panel is that there are more stars in the range of $|Z| > 2.5 \text{ kpc}$ (refer to Fig. 11). As age increases until 12 Gyr – 13.8 Gyr, there are more and more stars in the range $|Z| > 2.5 \text{ kpc}$, but stars in the range $-2.5 \text{ kpc} < Z < 2.5 \text{ kpc}$ become relatively fewer from 10 Gyr – 12 Gyr. We can see an almost uniform distribution for old stars in the 12 Gyr – 13.8 Gyr panel. This distribution is the same as findings by Hayden et al. (2015) for the thick disk.

In Figure 8, we can see the peaks in $|Z|$ change as a function of R for different ages quantitatively. For stars with age 0 Gyr – 2 Gyr, distribution of $|Z|$ decreases gradually from $|Z| \sim 0.8 \text{ kpc}$ to $|Z| \sim 0.1 \text{ kpc}$ with R from 5 kpc to 9 kpc. Moreover, the distribution is almost flat at $|Z| \sim 0.2 \text{ kpc}$ with R from 9 kpc to 15 kpc. For stars with age 12 Gyr – 13.8 Gyr, the distribution of $|Z|$ decreases gradually from $|Z| \sim 1.2 \text{ kpc}$ to $|Z| \sim 0.5 \text{ kpc}$ with R from 5 kpc to 9 kpc. However, the distribution increases from $|Z| \sim 0.5 \text{ kpc}$ to $|Z| \sim 2.2 \text{ kpc}$ with R from 9 kpc to 15 kpc. For stars in other age bins, distributions of $|Z|$ also manifest downward trends with R from 5 kpc to 9 kpc and increasing trends with R from 9 kpc to 15 kpc. The distributions of stars are more disperse for larger R in the range of $9 \text{ kpc} < R < 15 \text{ kpc}$. We also can see that older stars are distributed in higher regions, and younger stars are distributed in lower regions.

Figure 9 depicts the distribution of stars in Galactic coordinates (l, b) colored by $[\alpha/M]$ for different age bins. As we have found from Figure 6, for young stars from 0 Gyr – 2 Gyr, most of them have low- α abundance and few stars have high- α abundance. From panel a) (0 Gyr – 2 Gyr) of Figure 9, we can see these low- α stars are distributed in the low latitude region ($-30^\circ < \text{Latitude} < 30^\circ$) and a few stars which have high- α abundance are distributed in the high latitude region. As the age increases, more and more α -rich stars come out in the high latitude. Until 12 Gyr – 13.8 Gyr, i.e., old stars, most of these old stars are high- α stars. We find these high- α stars are distributed everywhere. Panel h) shows the distribution of all stars in the Galactic axis. We can see low- α stars are concentrated on the mid-plane and high- α stars are distributed in the high-latitude region.

Similar to Figure 9, we plot the distribution of stars in the (l, b) map in Figure 10 but here in bins of $[\alpha/M]$ and colored by age. From all these plots, we can clearly see the age of stars increases with the increase of $[\alpha/M]$ abundance. Stars are evenly distributed in the (l, b) map in each plot. In panel f), we plot all stars in the (l, b) map colored with age. Young stars are distributed in the low-latitude region and old stars are distributed in the high-latitude region. This distribution is the same as what Ho et al. (2017b) found before.

5 DISCUSSION

5.1 Our Data in View of Galactic Chemical Evolution Models

The relation of age with $[\alpha/M]$ and metallicity is broadly consistent with established expectations based on detailed studies of the solar neighborhood (Hayden et al. 2015; Xiang et al. 2017a). We show the theoretical evolution

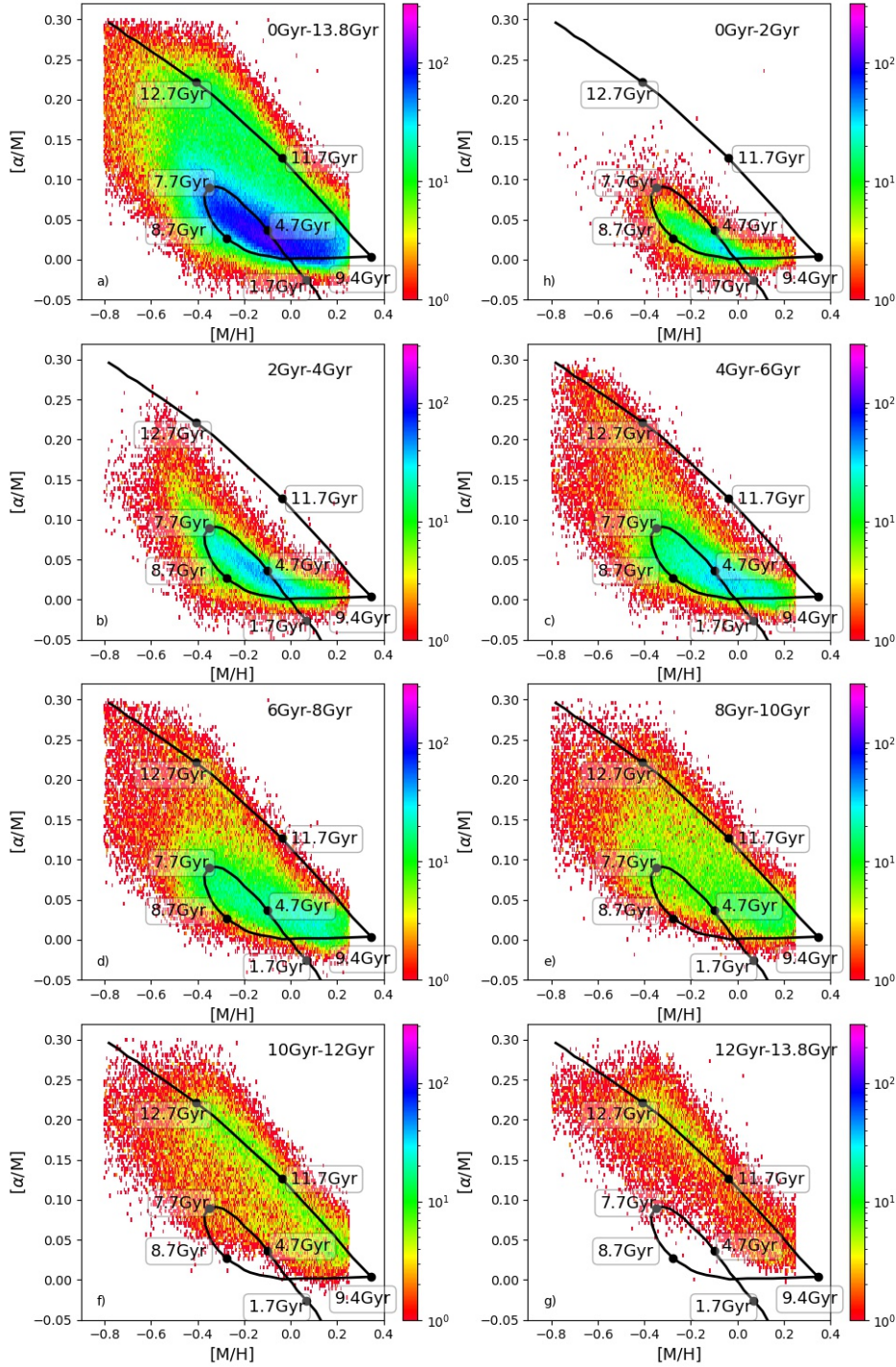


Fig. 6 Number density distribution of stars in the $[M/H]$ - $[\alpha/M]$ plane in different age bins. Colors indicate number density. Black lines signify revised two-infall model from Spitoni et al. (2019) for reference. In panel a), all stars from 0 Gyr to 13.8 Gyr are plotted. Two sequences of stars can be seen clearly. The low- α sequence is at $[M/H] \sim 0.0$ dex and $[\alpha/M] \sim 0.0$ dex and the high- α sequence is at $[M/H] \sim -0.5$ dex and $[\alpha/M] \sim 0.2$ dex. There are more stars in the low- α sequence than in the high- α sequence. In panel b), stars are mainly distributed at $[M/H] \sim 0.0$ dex and $[\alpha/M] \sim 0.0$ dex. In panel c), some stars with $[M/H] \sim -0.5$ dex and $[\alpha/M] \sim 0.2$ dex appear. In panel d), distribution of stars is similar to the distribution in panel b), but more stars appear at $[\alpha/M] \sim 0.20$ dex. In panel e), the distribution of stars is similar to the distribution in panel c), but more stars appear at $[\alpha/M] \sim 0.20$ dex. In panel f), the number of stars at $[M/H] \sim -0.1$ dex and $[\alpha/M] \sim 0.02$ dex is similar to the number of stars at $[M/H] \sim -0.5$ dex and $[\alpha/M] \sim 0.2$ dex. Stars are almost evenly distributed throughout the region. In panel g), few stars are distributed at $[M/H] \sim 0.0$ dex and $[\alpha/M] \sim 0.0$ dex. Most stars are distributed at $[M/H] \sim -0.5$ dex and $[\alpha/M] \sim 0.2$ dex. In panel h), stars are still mainly distributed at the $[M/H] \sim -0.5$ dex and $[\alpha/M] \sim 0.2$ dex region, but the number of stars is less than the number of stars in panel f).

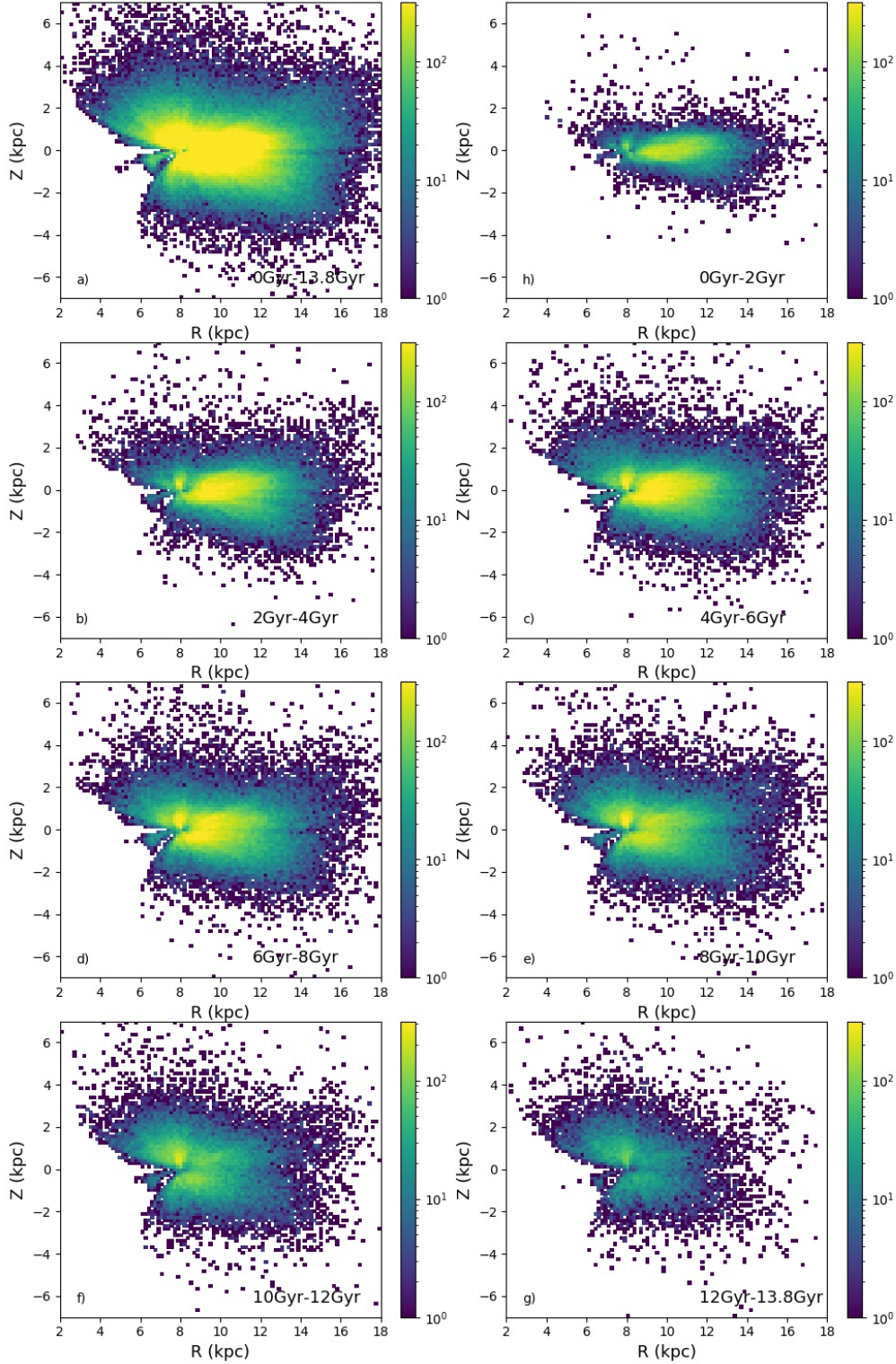


Fig. 7 Number density distribution of stars in the $R - Z$ plane in different age bins. Colors represent number density. In panel a), all stars from 0 Gyr to 13.8 Gyr are plotted. It features a dense region of stars extending from $R \sim 8.0$ kpc to $R \sim 16.0$ kpc. Most stars are distributed in the range of -3.0 kpc $< Z < 3.0$ kpc. In panel b), most young stars whose age is 0 Gyr – 2 Gyr are distributed in the range of -1.0 kpc $< Z < 1.0$ kpc. In panel c), most stars are distributed in the range of -1.0 kpc $< Z < 1.0$ kpc. However, some stars appear in the $|Z| > 2.0$ kpc region. In panel d), the distribution of stars is similar to the distribution in panel b), but more stars appear in the $|Z| > 2.0$ kpc region. In panel e), the distribution of stars is similar to the distribution in panel c), but the distribution of stars extends to the $|Z| \sim 3.0$ kpc region. In panel f), the dense region of stars extends to $R \sim 14.0$ kpc. Most stars are distributed in the range of -3.0 kpc $< Z < 3.0$ kpc. In panel g), stars are almost evenly distributed throughout the region. In panel h), stars are evenly distributed throughout the region.

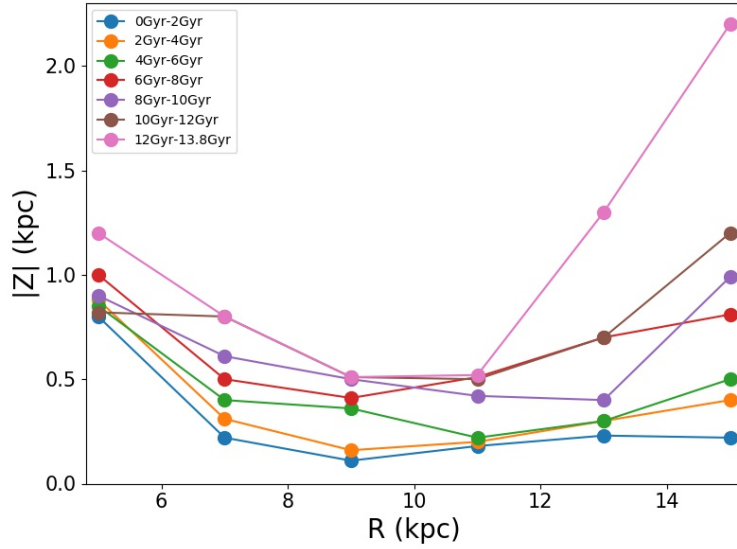


Fig. 8 Changes in the peaks of $|Z|$ as a function of R for different ages. Different colors represent stars in different age bins.

Table 1 Stellar Parameters of the First Ten Stars in the Catalog

obsid	R.A. (deg)	Decl. (deg)	T_{eff} (K)	$\log g$ (dex)	$[M/H]$ (dex)	$[\alpha/M]$ (dex)	X (kpc)	Y (kpc)	Z (kpc)	R (kpc)	Mass (M_{\odot})	Age (Gyr)
469802144	298.42	35.28	4921.27	2.61	0.12	0.00	1.09	3.15	0.22	7.75	1.93	0.70
469802131	298.28	35.30	4642.10	2.54	0.08	0.03	1.27	3.68	0.27	7.82	1.31	6.63
469802097	298.03	35.23	4660.30	2.47	0.18	0.00	1.38	3.95	0.30	7.86	1.47	4.84
469802076	297.91	35.25	4745.52	2.48	0.14	0.03	0.91	2.60	0.20	7.71	1.48	3.91
462405158	286.87	24.70	4901.91	2.41	0.24	0.10	2.02	3.08	0.49	6.88	1.03	4.55
462405165	286.96	24.75	4356.49	1.87	0.12	0.07	3.03	4.64	0.74	6.93	1.13	11.2
462505175	286.91	24.77	4970.09	2.50	0.17	0.09	1.35	2.08	0.33	7.12	1.30	2.30
462404143	286.93	24.81	4661.76	2.54	0.08	0.01	2.57	3.94	0.63	6.85	1.30	6.63
462404129	286.83	24.80	5030.41	2.37	0.76	0.26	2.62	4.02	0.65	6.85	1.11	6.01
462504147	286.83	24.85	4929.52	2.43	0.27	0.08	1.73	2.66	0.43	6.96	1.22	3.80

Notes: This table is available online. A portion is shown here for guidance regarding its form and content.

model named revised two infall model from Spitoni et al. (2019) in Figure 5 to make a comparison with observed data.

While the general trend of higher ages with higher $[\alpha/M]$ is recovered by the model, we see a significant disagreement in quantities. The youngest stars exhibit $[\alpha/M]$ of 0.00 dex in our data, whereas the model suggests a slightly subsolar $[\alpha/M]$ of -0.05 dex. This is likely caused by the incomplete low- α training data in the sample considered in our study. Data and model agree around ages of 4 Gyr – 8 Gyr, but whereas our data suggest a strict increase of $[\alpha/M]$ beyond 8 Gyr, the model suggests a drop (corresponding to the time of major infall). Above 10 Gyr, our data agree again.

When looking at the age-metallicity relation, we see good agreement between 0 Gyr and 8 Gyr, but our data do not hint at an increase in $[M/H]$ around 8 Gyr – 10 Gyr, as suggested by the revised two-infall model. Beyond this range, we cannot compare data and model due to the metallicity limit of our sample ($[M/H] > -0.75$ dex).

In the $[M/H]$ – $[\alpha/M]$ panels, for the oldest stars (10 Gyr – 13.8 Gyr), our data overlap extremely well with the Spitoni models above 10 Gyr. For 6 Gyr – 8 Gyr, we see stars in a similar $[M/H]$ regime as the revised two-infall model, but our $[\alpha/M]$ is typically 0.05 dex higher than the model. Below 8 Gyr, the location of the loop of $[\alpha/M]$ for the lowest $[M/H]$ predicted by the revised two-infall model agrees well with our data.

5.2 Galactic Vertical Scale Height as a Function of Age

We assume the distribution of stars in the Galaxy is symmetrical with respect to the Z axis, so we explore histograms of $|Z|$ for stars in different age bins in panel a) of Figure 11. For stars in the ranges of 0 Gyr – 2 Gyr, 2 Gyr – 4 Gyr and 4 Gyr – 6 Gyr, the peaks of $|Z|$ are close to 0 kpc. But for stars in the ranges of 6 Gyr – 8 Gyr, 8 Gyr – 10 Gyr and 10 Gyr – 12 Gyr, the peaks are nearly at 0.5 kpc. For stars in the range of 12 Gyr – 13.8 Gyr,

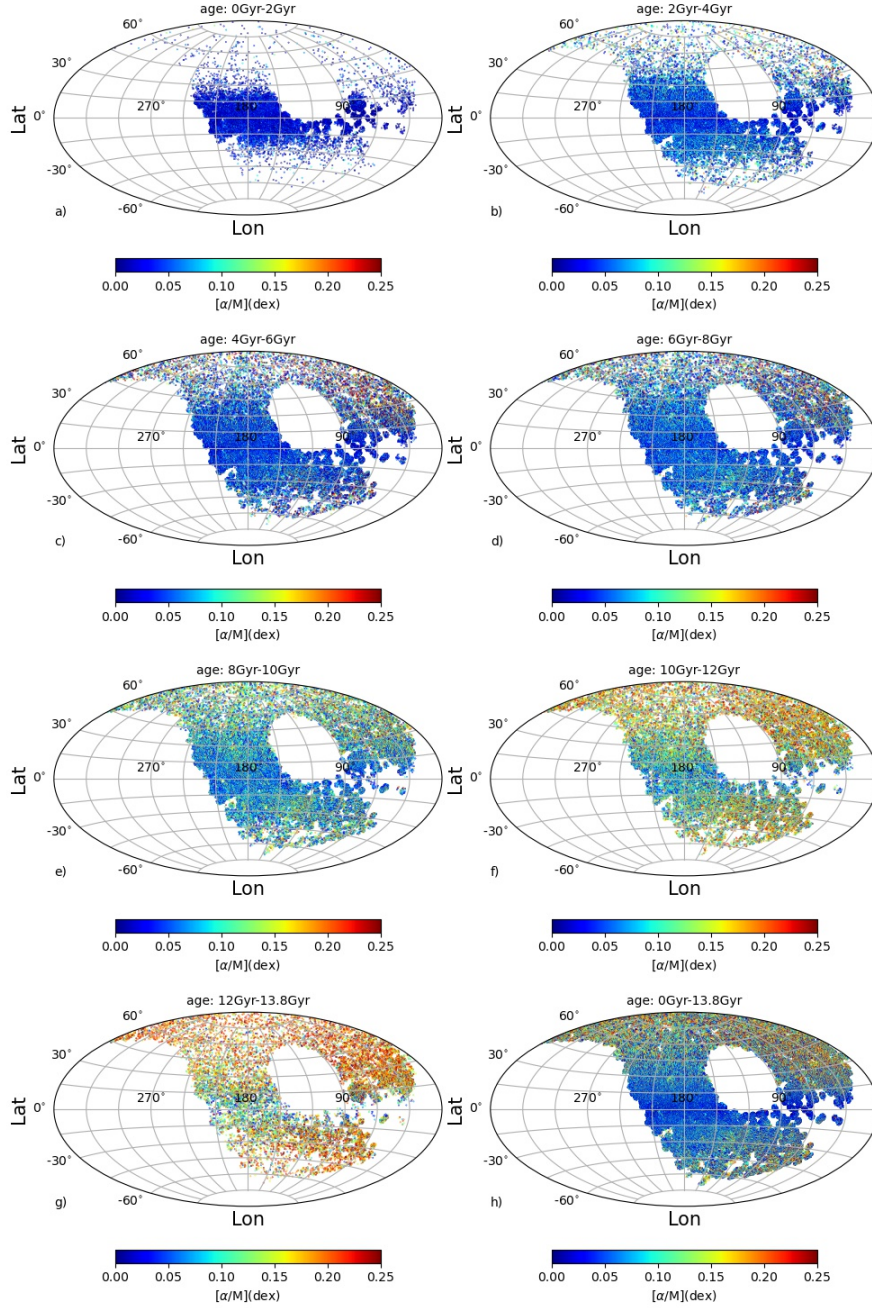


Fig. 9 Distribution of stars in the (l, b) map colored by $[\alpha/M]$ with 2 Gyr age steps. Colors represent $[\alpha/M]$. In panel a), most young stars whose age is 0 Gyr – 2 Gyr are distributed in the range of $-30^\circ < \text{Latitude} < 30^\circ$. $[\alpha/M]$ of these stars is close to 0.00 dex. In panel b), most stars with $[\alpha/M] \sim 0.00$ dex are distributed in the range of $-30^\circ < \text{Latitude} < 30^\circ$, but some stars with $[\alpha/M] \sim 0.10$ dex appear in the $|\text{Latitude}| > 30^\circ$ region. In panel c), distribution of stars is similar to the distribution in panel b), but some stars with $[\alpha/M] \sim 0.20$ dex are distributed in the $|\text{Latitude}| > 30^\circ$ region. In panel d), the distribution of stars is similar to the distribution in panel c), but more stars with $[\alpha/M] \sim 0.10$ dex are distributed in the $|\text{Latitude}| > 30^\circ$ region. In panel e), stars with $[\alpha/M] \sim 0.05$ dex are distributed in the $-30^\circ < \text{Latitude} < 30^\circ$ region. Stars with $[\alpha/M] \sim 0.20$ dex are distributed in the $|\text{Latitude}| > 30^\circ$ region. In panel f), a small number of stars with $[\alpha/M] \sim 0.05$ dex are distributed in the $-30^\circ < \text{Latitude} < 30^\circ$ region. Most stars with $[\alpha/M] \sim 0.20$ dex are distributed in the $|\text{Latitude}| > 30^\circ$ region. In panel g), almost all stars with $[\alpha/M] \sim 0.20$ dex are distributed in all regions. In panel h), all stars from 0 Gyr to 13.8 Gyr are plotted. It shows stars with $[\alpha/M] \sim 0.02$ dex are distributed in the $-30^\circ < \text{Latitude} < 30^\circ$ region and stars with $[\alpha/M] \sim 0.20$ dex are distributed in the $|\text{Latitude}| > 30^\circ$ region.

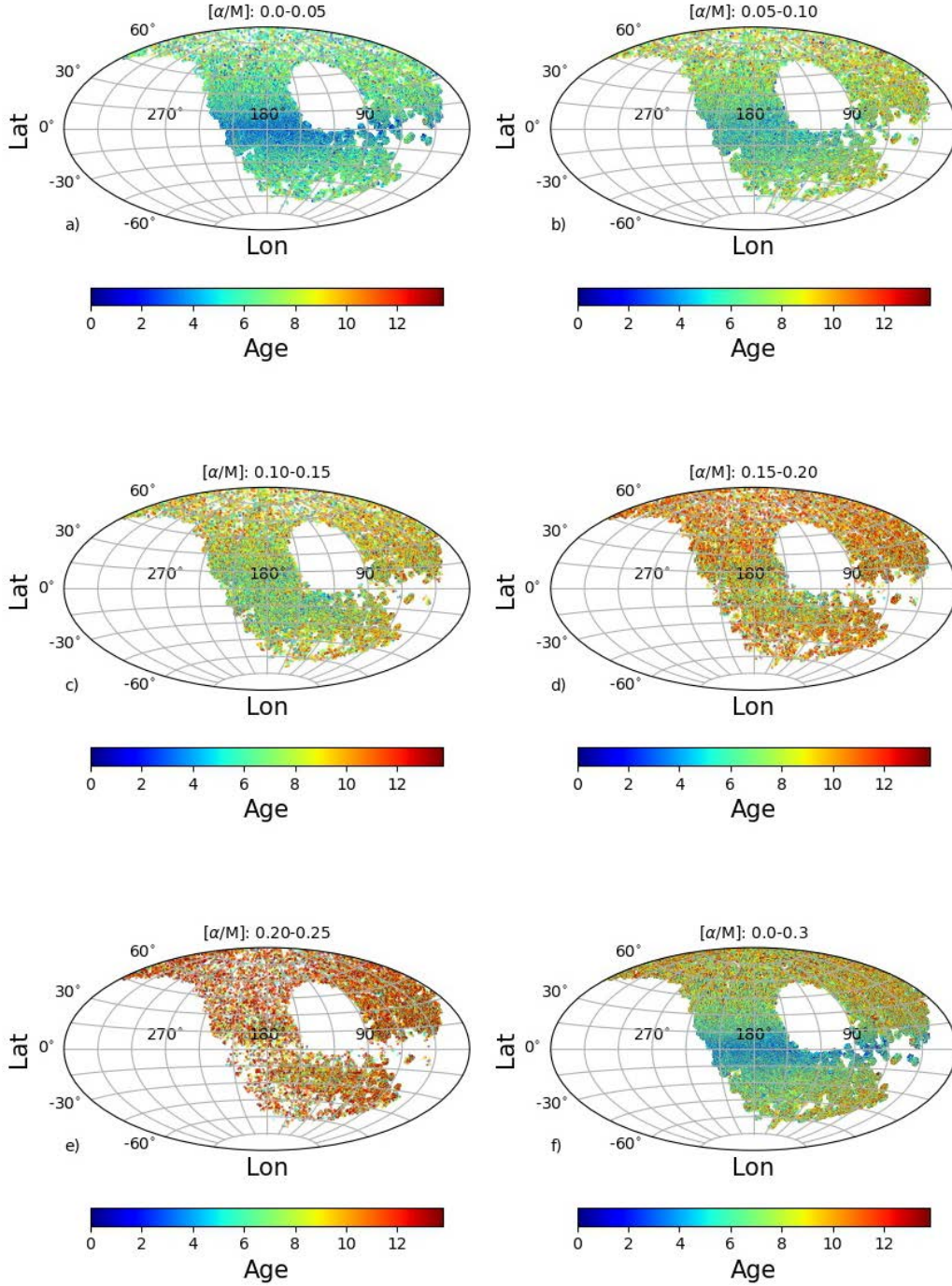


Fig. 10 Distribution of stars in the (l, b) map colored by age with 0.05 dex $[\alpha/M]$ steps. Colors indicate ages. In panel a), age of stars is in the range of 0 Gyr – 7 Gyr. Young stars whose age is ~ 2 Gyr are distributed in the range of $-30^\circ < \text{Latitude} < 30^\circ$. Stars with age ~ 6 Gyr are distributed in the $|\text{Latitude}| > 30^\circ$ region. In panel b), age of stars is in the range of 4 Gyr – 10 Gyr. Young stars whose age is ~ 4 Gyr are distributed in the range of $-30^\circ < \text{Latitude} < 30^\circ$. Stars with age ~ 8 Gyr are distributed in the $|\text{Latitude}| > 30^\circ$ region. In panel c), age of stars is in the range of 6 Gyr – 11 Gyr. Stars are distributed in all regions. In panel d), age of stars is in the range of 9 Gyr – 12 Gyr. Stars are distributed in all regions. In panel e), age of stars is in the range of 10 Gyr – 13.8 Gyr. Stars are distributed in all regions. In panel f), all stars from 0.0 dex to 0.3 dex are plotted. Young stars are distributed in the range of $-30^\circ < \text{Latitude} < 30^\circ$ while old stars are distributed in the range of $|\text{Latitude}| > 30^\circ$ region.

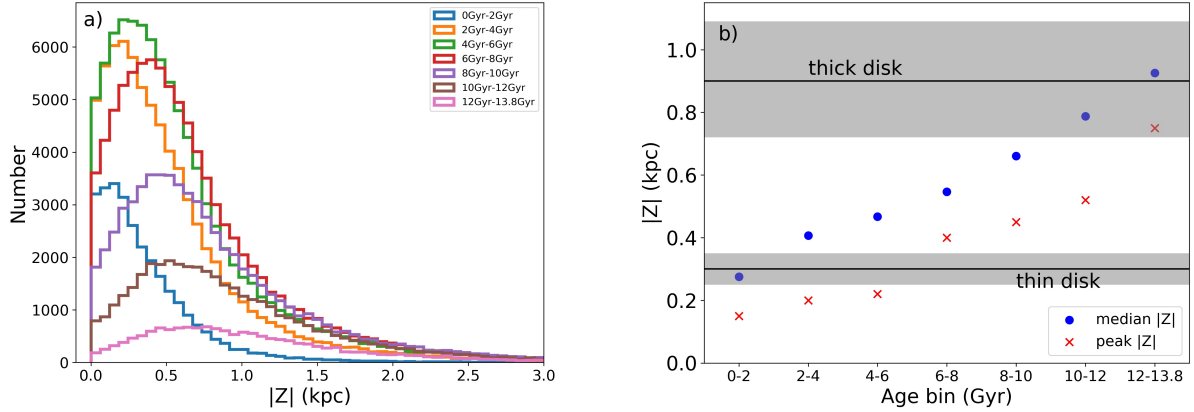


Fig. 11 Panel a): Histogram of $|Z|$ for stars in different age bins. Different colors correspond to stars in different age bins. Panel b): median values of $|Z|$ and peak values of $|Z|$ in different age bins. The *blue dots* represent median values and the *red crosses* signify peak values. *Grey color* represents the estimates of the thick and thin disk vertical scale length from Bland-Hawthorn & Gerhard (2016).

the peak is close to 1.0 kpc. Although we also report the median of the distribution, we rely on the peak position, as the distributions are highly skewed.

In panel b) of Figure 11, we also overplot the thin and thick disk vertical scale-heights, $z^t = 300 \pm 50$ pc and $z^T = 900 \pm 180$ pc, as reviewed by Bland-Hawthorn & Gerhard (2016). While we see that this scale-height agrees between the thin disk scale-height for stars with the stars of 2 Gyr – 6 Gyr, and the thick disk scale-height for stars above 12 Gyr, we see that our data disagree for the intermediate age (6 Gyr – 12 Gyr) and the youngest stars (with our data suggesting a smaller vertical scale length). This has important implications, as it suggests that the scale-length is not only population-dependent (that is thin/thick or low-/high- α population), but also strongly age-dependent.

5.3 Age-abundance Gradients with Galactic Height

In Figure 12, we display the metallicity gradient and α -enhancement gradient for stars in different age bins. With the increase of $|Z|$ from 0 kpc to 3 kpc, metallicity presents a decreasing trend for stars in every age bin. Metallicity decreases from ~ -0.1 dex to ~ -0.5 dex, which means there is a metallicity gradient from the Galactic plane to higher regions. With the increase of $|Z|$ from 0 kpc to 3 kpc, $[\alpha/M]$ presents an increasing trend for stars in every age bin. For 0 Gyr to 2 Gyr stars, $[\alpha/M]$ increases from ~ 0.02 dex to ~ 0.05 dex. For 2 Gyr to 4 Gyr stars, $[\alpha/M]$ increases from ~ 0.03 dex to ~ 0.12 dex. For 4 Gyr to 6 Gyr stars, $[\alpha/M]$ increases from ~ 0.03 dex to ~ 0.15 dex. For 6 Gyr to 8 Gyr stars, $[\alpha/M]$ increases from ~ 0.03 dex to ~ 0.15 dex. For 8 Gyr to 10 Gyr stars, $[\alpha/M]$ increases from ~ 0.06 dex to ~ 0.16 dex. For 10 Gyr to 12 Gyr stars, $[\alpha/M]$ increases from ~ 0.09 dex to ~ 0.18 dex. For 12

Gyr to 13.8 Gyr stars, $[\alpha/M]$ increases from ~ 0.13 dex to ~ 0.22 dex. The increasing trend means there is an α -enhancement gradient from the Galactic plane to higher regions. So, we think that young stars are close to the Galactic plane and stars which are old are on dynamically hot orbits.

6 CONCLUSIONS

In this study, we estimate stellar ages and masses for giant stars observed by LAMOST and use them to further the understanding of Galactic spatial and abundance gradients and their dependence on stellar age. We have considered 938 720 giants which have stellar parameters and α , C, N estimates from LAMOST DR5 v1 version (Zhang et al. 2019). These stellar parameters are compared with those from Xiang et al. (2018). Taking the bias offsets into account, we are utilizing the empirical formula estimated from the data by Xiang et al. (2018); 556 007 stars are selected with the empirical formula applied. We estimate ages and masses for these stars based on the $[C/N]$ abundance ratio and main stellar parameters. The age distribution of these stars ranges from 0 Gyr to 13.8 Gyr and mass distribution ranges from $0.8 M_{\odot}$ to $2.4 M_{\odot}$. Compared with ages and masses derived from the KPCA method (Wu et al. 2018), it yields uncertainty of 2.4 Gyr and bias of 1.1 Gyr in age, and uncertainty of $0.3 M_{\odot}$ and bias of $0.06 M_{\odot}$ in mass. Our age and mass estimates are also consistent with values from Martig et al. (2016) and Ness et al. (2016). Combining photogeometric distances (Bailer-Jones et al. 2021; Gaia Collaboration et al. 2020) and proper motions from Gaia EDR3 (Gaia Collaboration et al. 2020) and radial velocity from LAMOST DR5 (Luo et al. 2015; Wu et al. 2011), we get 3D coordinates

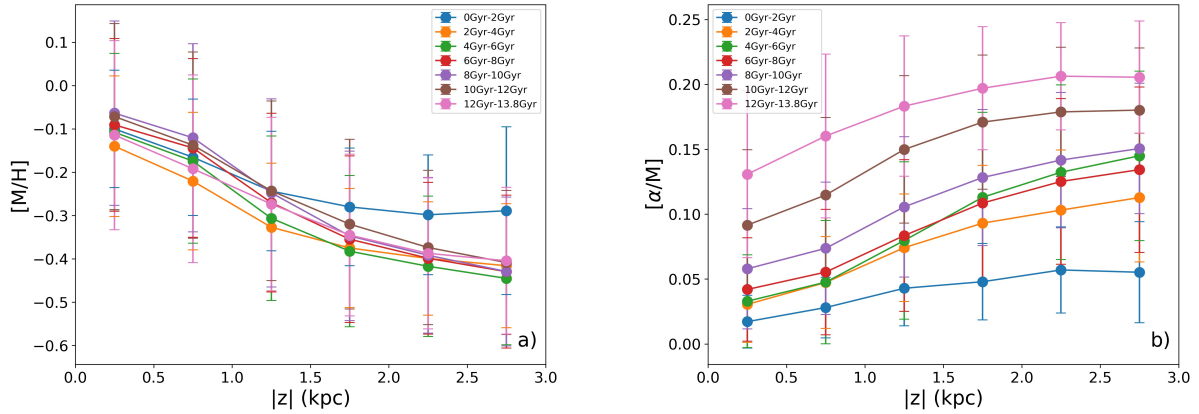


Fig. 12 Panel a): $[M/H]$ versus $|Z|$ for stars in different age bins. Different colors correspond to results for different age bins. Error bars for each age bin are also displayed. Panel b): $[\alpha/M]$ versus $|Z|$ for stars in different age bins.

(X, Y, Z) and galactocentric distances (R) for 419 038 stars.

With this large sample, we further investigated possible correlations among age, $[\alpha/M]$ and $[M/H]$. The age– $[\alpha/M]$ relation exhibits two separate sequences. The high- α sequence is dominated by stars older than 8 Gyr and the low- α sequence is composed of stars with a wide range of ages, from as young as 0 Gyr to older than 11 Gyr. There is a weak correlation between age and $[M/H]$ within the stellar disk populations. Two prominent sequences of chemical composition, consistent with the thin and thick disk sequence, are depicted in the $[M/H]$ – $[\alpha/M]$ panel with all stars from 0 Gyr – 13.8 Gyr.

We detect the spatial distribution of stars with 2 Gyr bins. The distributions of stars are more disperse in $|Z|$ for larger R in the range of $9 \text{ kpc} < R < 15 \text{ kpc}$. The much more extensive area coverage of the LAMOST data on the sky than previous spectroscopic survey is immediately apparent. Young stars are distributed in the low-latitude region while old stars are distributed in the high-latitude region.

Our observed data agree well with the Galactic Chemical Evolution model (Spitoni et al. 2019) from 4 Gyr to 8 Gyr and above 10 Gyr in the age– $[\alpha/M]$ relation, from 0 Gyr to 8 Gyr in the age– $[M/H]$ relation, and from 10 Gyr to 13.8 Gyr in the $[M/H]$ – $[\alpha/M]$ relation. There are the most stars in the range of 4 Gyr – 6 Gyr. With our age estimates and their uncertainties, we find a smooth transition of median Galactic height $|Z|$ for different age bins, with the median $|Z|$ of the youngest stars agreeing well with the canonical thin disk scale height, and the median $|Z|$ of the oldest stars agreeing well with the canonical thick disk, suggesting a strong age-dependence for Galactic scale height. We can detect the metallicity gradient and $[\alpha/M]$ -enhancement gradient in the $|Z|$ direction for stars in each age bin. So, we confirm

the conclusion that young stars are close to the Galactic plane and stars which are old are on dynamically hot orbits.

Acknowledgements We thank Yuqin Chen and Wenbo Wu for their helpful discussion. This study is supported by the National Natural Science Foundation of China (Grant Nos. 11988101, 11890694), and National Key R&D Program of China (No. 2019YFA0405502), and China Scholarship Council. X.Z. acknowledges hosting at the Australian National University for part of this research. The Guoshoujing Telescope (the Large sky Area Multi-Object Fiber Spectroscopic Telescope, LAMOST) is a National Major Scientific Project built by the Chinese Academy of Sciences. Funding for the project has been provided by the National Development and Reform Commission. LAMOST is operated and managed by the National Astronomical Observatories, Chinese Academy of Sciences.

References

- Asplund, M., Grevesse, N., Sauval, A. J., et al. 2009, *ARA&A*, 47, 481
- Bailer-Jones, C. A. L., Rybizki, J., Foesneau, M., et al. 2021, *AJ*, 161, 147
- Bergemann, M., et al. 2014, *A&A*, 565, A89
- Bensby, T., Feltzing, S., & Lundstrom, I. 2003, *A&A*, 410, 527
- Bland-Hawthorn, J., & Gerhard, O. 2016, *ARA&A*, 54, 529
- Bland-Hawthorn, J., Sharma, S., Tepper-Garcia, T., et al. 2019, *MNRAS*, 486, 1167
- Borucki, W. J., et al. 2010, *Science*, 327, 977
- Bovy, J. 2015, *ApJS*, 216, 29
- Buder, S., Lind, K., Ness, M. K., et al. 2019, *A&A*, 624, A19
- Buder, S., Sharma, S., Kos, J., et al. 2021, *MNRAS*, [doi:10.1093/mnras/stab1242](https://doi.org/10.1093/mnras/stab1242)
- Chiappini, C., Anders, F., Rodrigues, T. S., et al. 2015, *A&A*, 576, L12

- Cui, X.Q., Zhao, Y.H., Chu, Y.Q., et al. 2012, RAA (Research in Astronomy and Astrophysics), 12, 1197
- De Silva, G. M., et al. 2015, MNRAS, 449, 2604
- Fuhrmann, K. 1998, A&A, 338, 161
- Fabbro, S., Venn, K. A., Briain, T. O., et al. 2018, MNRAS, 475, 2978
- Gaia Collaboration, et al. 2021, A&A, 649, A1
- Gravity Collaboration, et al. 2018, A&A, 615, L15
- Hayden, M. R., et al. 2015, ApJ, 808, 132
- Haywood, M., Di Matteo, P., Lehnert, M. D., et al. 2013, A&A, 560, A109
- Ho, A. Y. Q., Ness, M. K., Hogg, D. W., et al. 2017a, ApJ, 836, 5
- Ho, A. Y. Q., Rix, H. W., Ness, M. K., et al. 2017b, ApJ, 841, 40
- Koleva, M., Prugniel, P., Bouchard, A., et al. 2009, A&A, 501, 1269
- Lee, Y. S. et al. 2011, ApJ, 738, 187
- Luo, A. L., Zhao, Y. H., Zhao, G., et al. 2015, RAA (Research in Astronomy and Astrophysics), 15, 1095
- Majewski, S. R., Schiavon, R. P., Frinchaboy, P. M., et al. 2017, AJ, 154, 94
- Masseron, T., & Gilmore, G. 2015, MNRAS, 453, 1855
- Martig, M., Fouesneau, M., Rix, H.-W., et al. 2016, MNRAS, 456, 3655
- Ness, M., Hogg, D. W., Rix, H.-W., et al. 2016, ApJ, 823, 114
- Nordstrom, B., et al. 2004, A&A, 418, 989
- O’Brian, T., Ting, Y. S., Fabbro, S., et al. 2021, ApJ, 906, 130
- Pinsonneault, M. H., et al. 2014, ApJS, 215, 19
- Reid, M. J., & Brunthaler, A. 2004, ApJ, 616, 872
- Schoenrich, R., Binney, J., & Dehnen, W. 2010, MNRAS, 403, 1829
- Sellwood, J. A., & Binney, J. J. 2002, MNRAS, 336, 785
- Sharma, S., Hayden, R. M., Bland-Hawthorn, J., et al. 2020, arXiv e-prints, arXiv:2011.13818
- Spitoni, E., Silva Aguirre, V., Matteucci, F., et al. 2019, A&A, 623, A60
- Soderblom, D. R. 2010, ARA&A, 48, 581
- Wu, Y., Luo, A.-L., Li, H.-N., et al. 2011, RAA (Research in Astronomy and Astrophysics), 11, 924
- Wu, Y., Xiang, M., Bi, S., et al. 2018, MNRAS, 475, 3633
- Wu, Y., et al. 2019, MNRAS, 484, 5315
- Xiang, M. S., et al. 2018, ApJS, 237, 33
- Xiang, M. S., et al. 2017a, MNRAS, 464, 3657
- Xiang, M. S., et al. 2017b, ApJS, 232, 2
- Zhao, G., Chen, Y. Q., Shi, J. R., et al. 2006, ChJAA (Chin. J. Astron. Astrophys.), 6, 265
- Zhao, G., Zhao, Y. H., Chu, Y. Q., et al. 2012, RAA (Research in Astronomy and Astrophysics), 12, 723
- Zhang, X., Zhao, G., Yang, C. Q., et al. 2019, PASP, 131, 094202